TU Delft

Delft University of Technology

Microstructure, mechanical, and corrosion properties of $Zr_{1-x}Cr_xB_y$ diboride alloy thin films grown by hybrid high power impulse/DC magnetron co-sputtering

Bakhit, Babak; Dorri, Samira; Kosari, Ali; Mol, Arjan; Petrov, Ivan; Birch, Jens; Hultman, Lars; Greczynski, Grzegorz

DOI
10.1016/j.apsusc.2022.153164

Publication date
2022

Document Version
Final published version

Published in
Applied Surface Science

Citation (APA)
Bakhit, B., Dorri, S., Kosari, A., Mol, A., Petrov, I., Birch, J., Hultman, L., & Greczynski, G. (2022). Microstructure, mechanical, and corrosion properties of $Zr_{1-x}Cr_xB_y$ diboride alloy thin films grown by hybrid high power impulse/DC magnetron co-sputtering. *Applied Surface Science*, *591*, Article 153164. https://doi.org/10.1016/j.apsusc.2022.153164

Important note
To cite this publication, please use the final published version (if applicable).
Please check the document version above.

Copyright
Other than for strictly personal use, it is not permitted to download, forward or distribute the text or part of it, without the consent of the author(s) and/or copyright holder(s), unless the work is under an open content license such as Creative Commons.

Takedown policy
Please contact us and provide details if you believe this document breaches copyrights.
We will remove access to the work immediately and investigate your claim.

This work is downloaded from Delft University of Technology.
For technical reasons the number of authors shown on this cover page is limited to a maximum of 10.

Applied Surface Science 591 (2022) 153164

Contents lists available at ScienceDirect

Applied Surface Science

journal homepage: www.elsevier.com/locate/apsusc

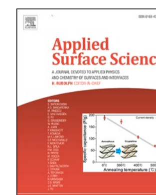

Full Length Article

Microstructure, mechanical, and corrosion properties of $Zr_{1-x}Cr_xB_y$ diboride alloy thin films grown by hybrid high power impulse/DC magnetron co-sputtering

Babak Bakhit [a,*], Samira Dorri [a], Ali Kosari [b], Arjan Mol [b], Ivan Petrov [a,c,d], Jens Birch [a], Lars Hultman [a], Grzegorz Greczynski [a]

[a] Thin Film Physics Division, Department of Physics (IFM), Linköping University, Linköping SE-58183, Sweden
[b] Department of Materials Science and Engineering, Delft University of Technology, Delft 2628CD, the Netherlands
[c] Materials Research Laboratory and Department of Materials Science, University of Illinois, Urbana, IL 61801, USA
[d] Department of Materials Science and Engineering, National Taiwan University of Science and Technology, Taipei 10607, Taiwan

ARTICLE INFO

Keywords:
Thin films
Zirconium diborides
Diboride alloys
Microstructure
Mechanical properties
Corrosion protection

ABSTRACT

We study microstructure, mechanical, and corrosion properties of $Zr_{1-x}Cr_xB_y$ coatings deposited by hybrid high-power impulse/DC magnetron co-sputtering (CrB_2-HiPIMS/ZrB_2-DCMS). Cr/(Zr + Cr) ratio, x, increases from 0.13 to 0.9, while B/(Zr + Cr) ratio, y, decreases from 2.92 to 1.81. As reference, $ZrB_{2.18}$ and $CrB_{1.81}$ layers are grown at 4000 W DCMS. $ZrB_{2.18}$ and $CrB_{1.81}$ columns are continual from near substrate toward the surface with open column boundaries. We find that the critical growth parameter to achieve dense films is the ratio of Cr^+-dominated ion flux and the (Zr + B) neutral flux from the ZrB_2 target. Thus, the alloys are categorized in two groups: films with $x < 0.32$ (low Cr^+/(Zr + B) ratios) that have continuous columnar growth, rough surfaces, and open column boundaries, and films with $x \geq 0.32$ (high Cr^+/(Zr + B) ratios) that Cr^+-dominated ion fluxes are sufficient to interrupt continuous columns, resulting in smooth surface and dense fine-grain microstructure. The pulsed metal-ion irradiation is more effective in film densification than continuous Ar^+ bombardment. Dense $Zr_{0.46}Cr_{0.54}B_{2.40}$ and $Zr_{0.10}Cr_{0.90}B_{1.81}$ alloys are hard (>30 GPa) and almost stress-free with relative nano-indentation toughness of 1.3 MPa$\sqrt{m}$ and 2.3 MPa$\sqrt{m}$, respectively, and remarkedly low corrosion rates (~1.0 × 10^{-6} mA/cm^2 for $Zr_{0.46}Cr_{0.54}B_{2.40}$ and ~ 2.1 × 10^{-6} mA/cm^2 for $Zr_{0.10}Cr_{0.90}B_{1.81}$).

1. Introduction

Zirconium diboride (ZrB_2) with high melting point (~3245 °C) [1] and hardness (ranging from 19.3 to 46.0 GPa) [2-8], classified as ultra-high temperature ceramics [9], is a promising material for long-term service in extreme conditions including temperatures above 2000 °C, hydrostatic pressure, drastic chemical reactivity, mechanical stress, and very high levels of heat and radiation gradients [9-11]. It typically crystallizes in a hexagonal AlB_2-type structure (P6/mmm, SG-191) where B atoms form graphite-like honeycomb sheets sitting between hexagonal-close-packed Zr layers [12]. The lattice parameters of ZrB_2 are 3.17 Å and 3.53 Å in the in-plane and out-of-plane directions, respectively [13]. Strong covalent bonding between Zr and B atoms as well as within the honeycomb B sheets provide their high melting point, stiffness, and hardness [14]. In addition, metallic bonding within the Zr layers results in good thermal and electrical conductivities [12]. These ceramic and metallic properties make ZrB_2 a good candidate for many applications. For instance, they are suitable for aerospace applications such as in rocket components, atmospheric reentries, jet engine turbines, propulsion systems, and sharp leading edges in hypersonic vehicles [9,11,15-17].

Refractory diboride coatings grown by magnetron sputtering have recently received increasing attention as a new class of hard ceramic coatings to replace transition-metal (TM) nitrides in many applications [4-6,18-27]. However, the use of sputter-deposited TM diboride coatings are very restricted because of several critical issues. Contrary to TM nitrides, ZrB_2 are line-compound, and deviations from stoichiometry can lead to the formation of second phases [2]. Sputter-deposited ZrB_y thin films are typically overstoichiometric with B/Zr (y) ratios > 2 (containing excess B) that can influence their phase stability at elevated

* Corresponding author.
E-mail address: babak.bakhit@liu.se (B. Bakhit).

https://doi.org/10.1016/j.apsusc.2022.153164
Received 18 February 2022; Received in revised form 16 March 2022; Accepted 20 March 2022
Available online 28 March 2022
0169-4332/© 2022 The Author(s). Published by Elsevier B.V. This is an open access article under the CC BY license (http://creativecommons.org/licenses/by/4.0/).

temperatures [4,6]. This issue can be effectively resolved by employing high-power impulse magnetron sputtering (HiPIMS) that exploits differences in the ionization probabilities between TM and B atoms and gas rarefaction effects in order to guide ion fluxes toward substrates [21].

The other critical issue of ZrB_2 thin films is their inherent brittleness [28]. We recently proposed a strategy to increase both hardness and toughness of ZrB_2 layers by alloying with Ta [4]. The $Zr_{1-x}Ta_xB_y$ alloy films were grown using a hybrid high power impulse/DC magnetron co-sputtering (Ta-HiPIMS/ZrB_2-DCMS) scheme. Hardness increases from ~ 35.0 GPa for $ZrB_{2.4}$ to ~ 42.0 GPa for $Zr_{0.7}Ta_{0.3}B_{1.5}$, with an increase in nanoindentation toughness from ~ 4.0 to ~ 5.2 MPa$\sqrt{m}$. This simultaneous enhancement in mechanical properties is due to a transition in their nanostructure from B-rich to Ta-rich column boundaries and the formation of a self-organized columnar core/shell nanostructure [4,19]. In addition, TMB_2 suffer from poor high-temperature oxidation resistance, which is a critical property for many aggressive environments [29,30]. They oxidize at temperatures < ~450 °C with oxidation products consisting of TMO_2 and B_2O_3 [31]. Contrary to bulk diborides, the B_2O_3 phase evaporates rapidly at temperatures > ~400 °C from overstoichiometric TMB_2 thin films. This leads to the formation of a highly porous oxide layer with no oxidation protection [20,32,33]. As also proved for TiN-based coatings, alloying diboride thin films with Al significantly improves their oxidation resistance properties [20].

The ever-increasing demand for enhanced coating properties such as high hardness, good toughness, low wear rates, and increased oxidation and corrosion resistance motivates the search for multifunctional materials. We previously reported on the growth of ZrB_2-rich $Zr_{1-x}Cr_xB_y$ thin films using hybrid Cr-HiPIMS/ZrB_2-DCMS co-sputtering. Decreasing the ZrB_2 target power operated at DCMS mode (P_{ZrB_2}) leads to an increase in the Cr metal fraction x, Cr/(Zr + Cr), up to x = 0.44, while a decrease in the B/(Zr + Cr) ratio y from 2.18 to 1.11 due to both Cr addition and preferential B resputtering. The alloy films with x = 0.23 and 0.29 showed the highest hardness values, but their cube-corner nanoindentation impressions revealed brittle behavior. Increasing the Cr concentration (x > 0.29) resulted in enhanced ductility, wear, and corrosion resistance. However, it also caused a significant decrease of ~ 12 GPa in hardness. In addition, the alloys with x ≥ 0.36 were amorphous [18].

To retain the diboride lattice structure and thus avoid deterioration of mechanical properties, both caused by B deficiency, here, we use a CrB_2 target instead of Cr to grow the $Zr_{1-x}Cr_xB_y$ thin films by hybrid CrB_2-HiPIMS/ZrB_2-DCMS co-sputtering with metal-ion-synchronized substrate potential, and study the effect of CrB_y addition on their microstructure, mechanical, and corrosion properties. We demonstrate that the hybrid growth scheme enables to cover broad compositional range y = B/(Zr + Cr) from 2.90 to 1.81 for x = Cr/(Zr + Cr) varied from 0 to 1, which was hitherto not achievable by conventional DCMS processing. All alloy coatings show hexagonal crystal structure (solid solution) and have nanoindentation hardness values ranging from ~ 27.0 to ~ 32.5 GPa. Our results reveal that the hybrid co-sputtering technique that provides intense metal ion fluxes, resulting in dense layers with smooth surfaces, is favorable to DCMS, as long as the metal ion-flux density is sufficiently high with respect to the neutral flux from the DCMS-operated source.

2. Material and methods

$Zr_{1-x}Cr_xB_y$ thin films, in which x = Cr/(Zr + Cr) and y = B/(Zr + Cr), are grown in a CC800/9 CemeCon AG sputtering system (featuring integrated HiPIMS and DCMS power supplies) using cast rectangular 8.8 × 50 cm^2 stoichiometric ZrB_2 and CrB_2 targets. Al_2O_3(0001) and Si(001) are used as substrates. The Si(001) substrates are used for structural studies, while the Al_2O_3(0001) substrates are used for nanoindentation and residual stress measurements. The distance between the targets and substrates is 20 cm. The substrate temperature before starting the film growth is fixed at ~ 475 °C. The sputtering-system base pressure is 3.0 × 10^{-6} Torr (0.4 mPa). The films are deposited with an Ar pressure P_{Ar} = 3 mTorr (0.4 Pa).

The $Zr_{1-x}Cr_xB_y$ alloy films are grown using a hybrid CrB_2-HiPIMS/ZrB_2-DCMS scheme with metal-ion-synchronized substrate potential [34]. The ZrB_2 target is operated in DCMS mode, while the CrB_2 target is operated in HiPIMS mode, providing effective ion subplantation into DCMS-grown layers [35]. In order to cover a wide compositional range on the metal lattice, two series of $Zr_{1-x}Cr_xB_y$ alloy films are grown. First, at a constant CrB_2-HiPIMS-target average power (here, "average" refers to the entire cycle, i.e., including the pulse off time), frequency, and pulse width (950 W, 100 Hz, and 50 μs), the Cr metal fraction, x, increases from 0.13 to 0.17 to 0.24 by decreasing P_{ZrB_2} from 4000 W to 3000 W to 2000 W, respectively. In addition, while maintaining the average power, pulse width, and frequency applied to the HiPIMS CrB_2 target constant at 3400 W, 50 μs, and 300 Hz, respectively, the Cr metal fraction (y) increases from 0.32 to 0.90 by decreasing P_{ZrB_2} from 4000 W to 400 W. For both HiPIMS deposition conditions, the average peak CrB_2-target current density is ~ 1.0 A/cm^2 to provide high ionization of the sputtered flux [36]. A substrate potential of −100 V synchronized to the metal-rich portion of each HiPIMS pulse is employed (a 100-μs bias pulse with a 35-μs delay with respect to each HiPIMS pulse) [37]. In addition, ZrB_y and CrB_y reference thin films are deposited by DCMS with a target power of 4000 W at two different substrate bias conditions; (i) a floating substrate potential (-10 V) and (ii) a DC substrate potential (-100 V). Monte Carlo TRIM simulations are performed for better understanding the effects of metal ion irradiation.

Film elemental compositions are determined using time-of-flight elastic recoil detection analyses (ToF-ERDA). The ToF-ERDA measurements are carried out in a tandem accelerator with a 36 MeV $^{127}I^{8+}$ probe beam incident at 67.5° with respect to the sample surface normal. Recoils are detected at 45°. A Philips XPert X-ray diffractometer operated with a Cu-K_α source (λ = 0.15406 nm) is used to conduct X-ray diffraction (XRD) θ-2θ scans to obtain the crystal structure as well as orientations. A Zeiss LEO1550 scanning electron microscope (SEM) is employed to determine the layers' cross-sectional morphologies and thicknesses. Cross-sectional and plan-view transmission electron microscopy (TEM) analyses are carried out in a FEI Tecnai G^2 TF 20 UT instrument operated at 200 kV.

The residual stresses σ_f of the films are determined from substrate wafer curvatures using the modified Stoney equation (more details are given in References [38,39]). Nanoindentation analyses are carried out in an Ultra-Micro Indentation System equipped with a Berkovich diamond tip. The values of hardness H and elastic modulus E are determined by indenting the layers grown on Al_2O_3(0001) using a load of 11 mN. E values are calculated from reduced elastic moduli using the diamond indenter's elastic modulus (1141 GPa) and Poisson's ratio ν = 0.07. The ν values of $Zr_{1-x}Cr_xB_y$ required for obtaining E are unknown and estimated based upon a linear interpolation between the Poisson ratio of ZrB_2 (0.13 [40,41]) and that of CrB_2 (0.21 [41]).

The films grown on Al_2O_3(0001) are also indented by a diamond cube-corner tip in order to determine their relative nanoindentation toughness K_c. The cube-corner tip is a three-sided indenter similar to Berkovich tips, but sharper. Thus, it provides much higher local stresses that can significantly reduce the cracking threshold; suitable for inducing well-developed redial cracks at low loads, particularly in brittle materials [42]. The K_c values are estimated by measuring the average lengths of radial cracks around sample indents induced with the diamond cube-corner tip over a load range from 10 to 50 mN. Five indents are made at each load.

Electrochemical behavior of the thin films is assessed with a Bio-logic VSP-300 potentiostat/galvanostat system using an Ag/AgCl electrode as reference electrode, a Pt mesh as counter electrode, and the films as working electrode (a three-electrode corrosion setup). All measurements are carried out in a stationary 1.0 M NaCl corrosive medium without applying external heating. The open circuit potential E_{ocp} values are monitored versus the potential of the Ag/AgCl reference electrode. After

1-hour immersion, electrochemical impedance spectroscopy (EIS) measurements are performed in the frequency range of 100 kHz to 0.1 Hz with an amplitude of 10 mV at E_{ocp}. The potentiodynamic polarizations are then performed from −50 mV to 1200 mV with respect to E_{ocp} using a sweeping rate of 1 mV/s. The corrosion potentials E_{corr} and current densities i_{corr} are calculated from Tafel extrapolations.

3. Results and discussion

3.1. Composition and microstructure

Fig. 1 shows B/(Zr + Cr) and Cr/(Zr + Cr) ratios in $Zr_{1-x}Cr_xB_y$ thin films. The B/(Zr + Cr) ratios, y, in the $Zr_{1-x}Cr_xB_y$ alloy films deposited using hybrid CrB_2-HiPIMS/ZrB_2-DCMS co-sputtering with the HiPIMS CrB_2-target average power of 950 W (pulse frequency of 100 Hz) increases from 2.81 for P_{ZrB_2} = 2000 W to 2.92 for P_{ZrB_2} = 4000 W. For the alloys grown with the HiPIMS CrB_2-target average power of 3400 W (pulse frequency of 300 Hz), the y value gradually increases from 1.81 for P_{ZrB_2} = 400 W to 2.80 for P_{ZrB_2} = 4000 W. Overall, the B contents in the films deposited by the hybrid technique varies in the range from 2.92 to 1.81. In contrast, the y-values, in the ZrB_y and CrB_y films grown using DCMS at 4000 W and a DC substrate potential of −100 V, Fig. 1(a), span a narrower range of 2.18 and 1.8.

The Cr metal fraction, x, in the alloys deposited with the HiPIMS-CrB_2-target average power of 950 W (pulse frequency of 100 Hz) decreases from 0.24 for P_{ZrB_2} = 2000 W to 0.13 for P_{ZrB_2} = 4000 W, Fig. 1(b). For the $Zr_{1-x}Cr_xB_y$ alloys grown with the HiPIMS-CrB_2-target average power of 3400 W (pulse frequency of 300 Hz), the x value significantly decreases from 0.90 for P_{ZrB_2} = 400 W to 0.32 for P_{ZrB_2} = 4000 W.

The B/(Zr + Cr) ratio, y, is plotted versus the Cr metal fraction, x, in Fig. 1(c). For $Zr_{1-x}Cr_xB_y$ alloy films grown in a hybrid scheme, y shows a gradual decrease from 2.90 to 1.81 as the fraction of DCMS-sputtered flux from the ZrB_2 target (arriving at the self-bias potential) in the total material flux to the substrate decreases. Thus, the hybrid growth scheme with metal-ion-synchronized substrate potential offers the ability to tune the film composition over very wide range, including the possibility for stoichiometric diboride around x = ~0.8. For comparison, we deposited reference DCMS ZrB_y and CrB_y thin films using a DC substrate potential of −100 V, data points shown in Fig. 1(c), which indicate that the B/metal ratio can be varied in a much narrower range, from 2.18 to 1.8.

In order to assess the effect of substrate potential on the B/metal ratios, the ZrB_y and CrB_y thin films are also deposited using 4000-W DCMS with a floating substrate potential of −10 V, which results in y = 3.2 and 1.7, respectively. Thus, we find a very strong effect of energetic bombardment on the B concentration in the case of the Zr-containing film, with only minor effect in the case of the CrB_2 layer. This interesting result can be explained by the large mass-mismatch between the ions, predominantly Ar in this case (M_{Ar} = 40 amu) and Zr (M_{Zr} = 92.1 amu) that leads to the larger probability of backscattering of the ions (TRIM [43] simulations estimates the backscattering yield of ~ 6.8% with an energy up to ~ 15 eV). Energetic backscattered Ar may sputter B on the way back. For comparison, 100-eV Ar backscattering yield from Cr is only 0.07%, with a maximum energy that is below ~ 2 eV. This observation explains the large effect of DC substrate potential on the B concentration in the case of ZrB_y films and the minor effect for CrB_y layers. When we switch to predominantly Cr ion irradiation during the deposition of the alloy films in hybrid CrB_2-HiPIMS/ZrB_2-DCMS configuration, the maximum backscattered energy of 100 eV Cr^+ from Zr drops to ~ 7.5 eV, which together with the fact that the energetic flux constitutes a small portion of the HiPIMS pulse period (1–3 %), leads to a limited decrease in the B concentration in the Zr-rich alloy films, ~ 0.1 ≤ x ≤ ~0.2. As the alloy film becomes more Cr-rich, they retain less B and eventually reach the CrB_y value of y = 1.81.

Measuring the oxygen concentration after exposing the samples to

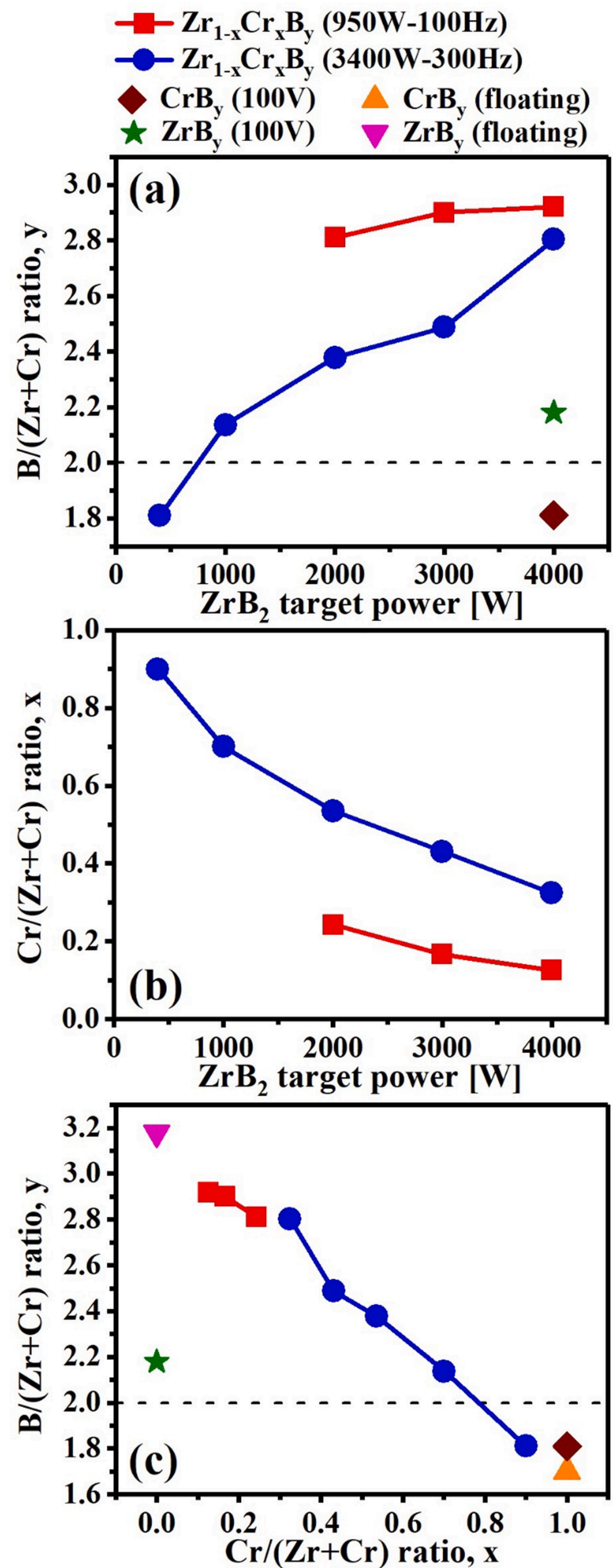

Fig. 1. (a) B/(Zr + Cr) ratios, y, (b) Cr/(Zr + Cr) ratios, x, in $Zr_{1-x}Cr_xB_y$ thin films as a function of ZrB_2 target power P_{ZrB_2}, and (c) corresponding B/(Zr + Cr) versus Cr/(Zr + Cr) ratios.

air is an indirect approach that in addition to direct methods, like TEM, can be employed for evaluating the film densification. Upon exposure to ambient atmosphere, oxygen penetrates into the open column boundaries and contributes to a high oxygen concentration in porous films. If the films are dense, the oxygen concentrations measured ex-situ are indicative of the oxygen incorporation during film growth under high vacuum conditions. This approach has been applied for assessing the effect of metal ion irradiation on increasing the densification of TM nitride thin films obtained by hybrid HiPIMS/DCMS co-sputtering [44-46]. Fig. 2 shows the ex-situ ToF-ERDA-measured oxygen concentration in $Zr_{1-x}Cr_xB_y$ alloys grown by CrB_2-HiPIMS/ZrB_2-DCMS plotted as a function of Cr/(Zr + Cr) ratio, x. For x ≤ 0.24, the oxygen concentration is relatively high, from 1.5 at. % to 2.1 at. %, indicative of residual porosity (oxygen incorporation during film growth under present conditions accounts for < 0.2 at. % [4,5,18,47]). This occurs since these layers are grown at lower HiPIMS frequency of 100 Hz (necessary to reach low x), hence with a very low substrate potential duty cycle of only 1%. Consequently, majority of the film-forming species (the ZrB_2 flux) is deposited at the self-bias potential condition, which does not provide enough adatom mobility, necessary for densification. The oxygen content, however, decreases abruptly to ≤ 0.2 at. % for the films grown with 300 Hz, and we find a range of compositions, 0.32 < x < 0.9, where dense alloys are obtained, as evidenced by the low oxygen concentration. The reference $ZrB_{2.18}$ and $CrB_{1.81}$ films deposited with −100 V DC substrate potentials show an increased level of oxygen; 1.5 and 0.8 at. %, respectively. The oxygen concentrations in the $ZrB_{3.2}$ and $CrB_{1.7}$ layers grown with self-bias potentials are even higher; 5.1 and 1.5 at. %, respectively. Thus, fully-dense layers are only obtained with the hybrid growth scenario, provided that the substrate potential duty cycle is sufficiently high. The concentration of Ar is ≤ 0.3 at. % in all coatings grown with −100 V substrate potential.

θ-2θ scans of $Zr_{1-x}Cr_xB_y$ thin films are shown in Fig. 3. All $Zr_{1-x}Cr_xB_y$ alloy films are crystalline as evidenced by strong XRD reflections from the crystalline hexagonal structure (solid solution). The positions of (000*l*) reflections move toward higher 2θ values that corresponds to a decrease in the out-of-plane (*c*) lattice parameter due mainly to the smaller size of Cr atoms incorporated in the diboride and the variation of residual stress levels. This lattice parameter gradually decreases from 3.535 Å for $ZrB_{2.18}$ to 3.045 Å for $CrB_{1.81}$ thin films as a function of the Cr concentration. The ($10\bar{1}0$) reflection disappears by alloying the $ZrB_{2.18}$ film with Cr. In addition, the ($10\bar{1}1$) peak intensity decreases by increasing Cr concentration up to x = 0.32, and this reflection disappears for the alloys with x > 0.32.

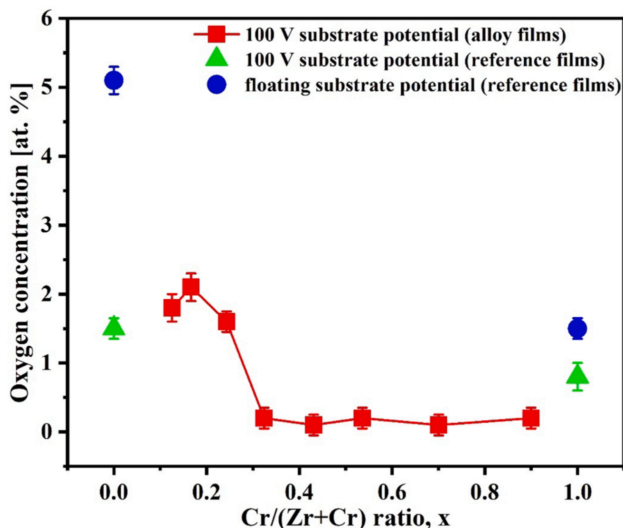

Fig. 2. Oxygen concentration in $Zr_{1-x}Cr_xB_y$ thin films as a function of Cr/(Zr + Cr) ratio, x.

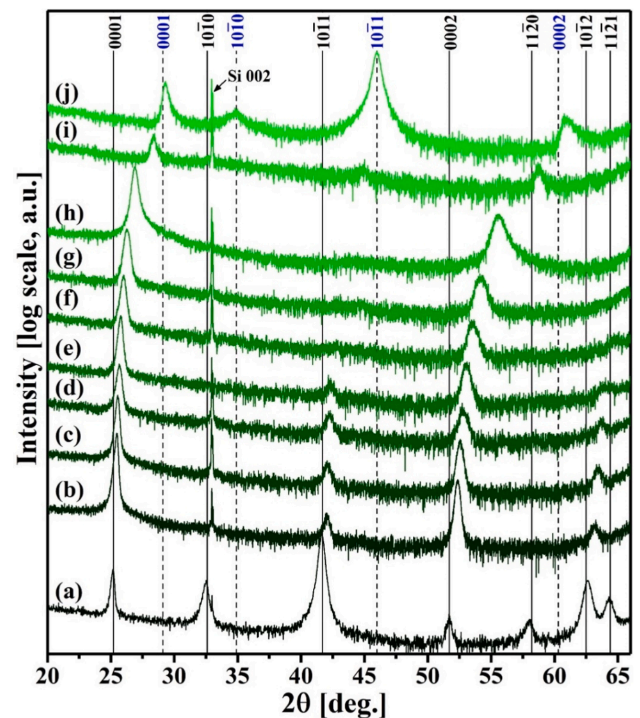

Fig. 3. θ-2θ scans of (a) $ZrB_{2.18}$, (b) $Zr_{0.87}Cr_{0.13}B_{2.92}$, (c) $Zr_{0.83}Cr_{0.17}B_{2.90}$, (d) $Zr_{0.76}Cr_{0.24}B_{2.81}$, (e) $Zr_{0.68}Cr_{0.32}B_{2.80}$, (f) $Zr_{0.57}Cr_{0.43}B_{2.50}$, (g) $Zr_{0.46}Cr_{0.54}B_{2.40}$, (h) $Zr_{0.30}Cr_{0.70}B_{2.14}$, (i) $Zr_{0.10}Cr_{0.90}B_{1.81}$, and (j) $CrB_{1.81}$ thin films grown on Si (001) substrates. Vertical solid and dashed lines correspond to reference powder-diffraction peak positions for ZrB_2 [13] and CrB_2 [48], respectively. The peak at 32.8° is a forbidden 002-substrate reflection [49].

The increase of Cr metal fraction, x = Cr/(Zr + Cr), on the cation sublattice also significantly increases the full-width-at-half-maximum (FWHM) values of the XRD peaks that can be primarily attributed to a smaller size of coherently diffracting domains and an increase in microstrains. For example, the FWHM value of the (0001) reflection increases from 0.387° for x = 0 to 0.852° for x = 0.70, whereas it decreases to 0.444° for x = 0.90 and 0.658° for x = 1.0. While the ($10\bar{1}1$) reflections are dominant peaks in the XRD patterns of $CrB_{1.81}$ and $ZrB_{2.18}$, the dominant peaks are (000*l*) for the $Zr_{1-x}Cr_xB_y$ alloy films.

Fig. 4 compares cross-sectional and plan-view SEM images of $ZrB_{2.18}$, $Zr_{0.87}Cr_{0.13}B_{2.92}$, $Zr_{0.68}Cr_{0.32}B_{2.80}$, $Zr_{0.46}Cr_{0.54}B_{2.40}$, $Zr_{0.10}Cr_{0.90}B_{1.81}$, and $CrB_{1.81}$ thin films. The SEM images of other alloys are not shown here since they exhibit similar microstructures to the layers presented in Fig. 4. All films are 2400 ± 55 nm thick. The cross-sectional SEM (XSEM) images in Fig. 4(a), 4(b), and 4(f) show that $ZrB_{2.18}$, $Zr_{0.87}Cr_{0.13}B_{2.92}$, and $CrB_{1.81}$ have a columnar microstructure. The columns are wide and extend through the films, while the microstructures of $Zr_{0.68}Cr_{0.32}B_{2.80}$, $Zr_{0.46}Cr_{0.54}B_{2.40}$, and $Zr_{0.10}Cr_{0.90}B_{1.81}$ alloy films consist of very fine columns that do not extend throughout the whole films, Fig. 4(c), 4(d), and 4(e). In addition, the XSEM images reveal that the $Zr_{0.68}Cr_{0.32}B_{2.80}$, $Zr_{0.46}Cr_{0.54}B_{2.40}$, and $Zr_{0.10}Cr_{0.90}B_{1.81}$ alloys have denser microstructures than $ZrB_{2.18}$, $Zr_{0.87}Cr_{0.13}B_{2.92}$, and $CrB_{1.81}$. This agrees with the ToF-ERDA-derived oxygen concentrations in these films which are at ~ 0.2 at. %, while the corresponding numbers for $ZrB_{2.18}$, $Zr_{0.87}Cr_{0.13}B_{2.92}$, and $CrB_{1.81}$ are ~ 1.5 at. %, ~2.1 at. %, and ~ 1.2 at. %, respectively.

$ZrB_{2.18}$ columns are inclined (~7°) with respect to the substrate normal in the direction of flux coming from the ZrB_2 target, which has an angle of 21° with respect to the substrates. However, the $Zr_{0.87}Cr_{0.13}B_{2.92}$ alloy has columns that are aligned along the substrate normal, similar to the typical growth of sputter-deposited thin films

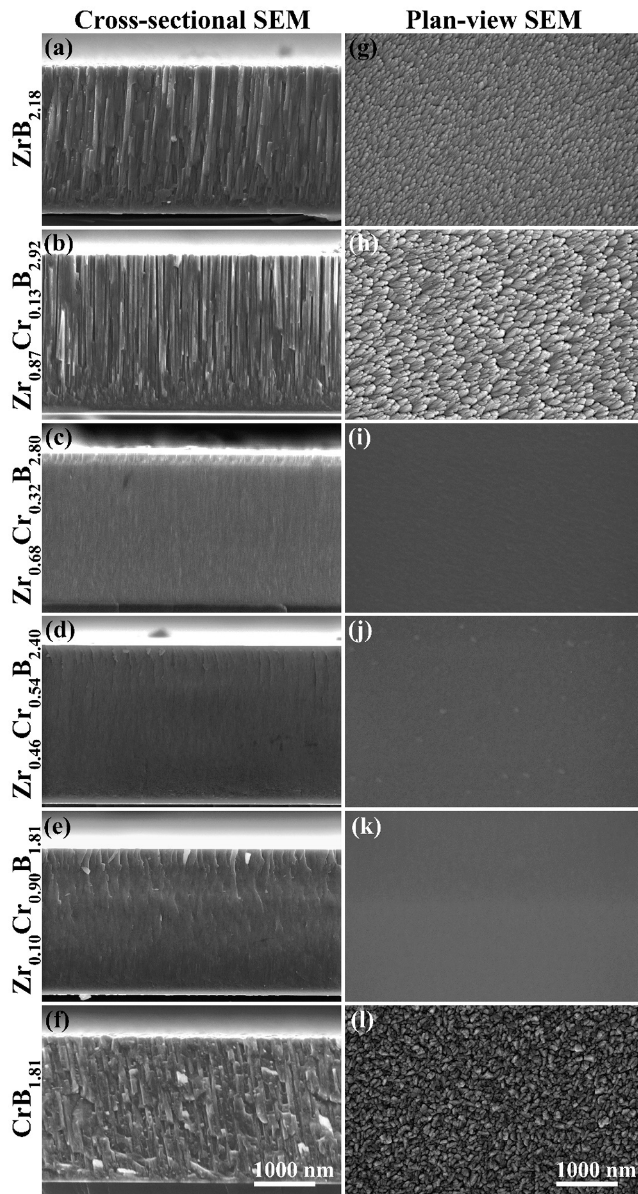

Fig. 4. Cross-sectional and plan-view SEM images of (a and g) $ZrB_{2.18}$, (b and h) $Zr_{0.87}Cr_{0.13}B_{2.92}$, (c and i) $Zr_{0.68}Cr_{0.32}B_{2.80}$, (d and j) $Zr_{0.46}Cr_{0.54}B_{2.40}$, (e and k) $Zr_{0.10}Cr_{0.90}B_{1.81}$, and (f and l) $CrB_{1.81}$ thin films.

where substrates face targets. The change observed in the columnar growth direction results from employing Cr^{+} ion irradiation during the deposition, where the energetic ions steered by the electric potential near the substrate arrive at the surface along the substrate normal and enhance atomic displacement [50]. In similarity to $ZrB_{2.18}$, the columns of the $CrB_{1.81}$ film are also inclined ($\alpha = \sim 7^{\circ}$) with respect to the substrate normal, but in opposite direction – toward the CrB_2 target.

The plan-view SEM images in Fig. 4(g)-4(l) show that $Zr_{0.68}Cr_{0.32}B_{2.80}$, $Zr_{0.46}Cr_{0.54}B_{2.40}$, and $Zr_{0.10}Cr_{0.90}B_{1.81}$ have significantly smoother surfaces than the $ZrB_{2.18}$, $Zr_{0.87}Cr_{0.13}B_{2.92}$, and $CrB_{1.81}$ films. Both $ZrB_{2.18}$ and $Zr_{0.87}Cr_{0.13}B_{2.92}$ layers have feather-like surface morphologies, where the features are inclined. There is also an increase in the feature sizes from $ZrB_{2.18}$ to the $Zr_{0.87}Cr_{0.13}B_{2.92}$ alloy. Opposite to these layers, the surface morphology of the $CrB_{1.81}$ film appears rough, consisting of granular features with different sizes and shapes. Fig. 4(i), 4(j), and 4(k) exhibit that the $Zr_{0.68}Cr_{0.32}B_{2.80}$, $Zr_{0.46}Cr_{0.54}B_{2.40}$, and $Zr_{0.10}Cr_{0.90}B_{1.81}$ alloy films have featureless, smooth surface morphologies.

Thus, the $Zr_{1-x}Cr_xB_y$ alloy films can be categorized in two groups: (i) the layers with $x < 0.3$ that have uninterrupted columnar growth, rough surfaces, and open column boundaries, which retain oxygen upon air exposure, and (ii) the layers with $x > 0.3$ that have dense microstructures, smooth surfaces, and low oxygen contents. Hence, we further study the nanostructure of representative sample from each group together with reference $ZrB_{2.18}$ and $CrB_{1.81}$ films using TEM.

Cross-sectional bright-field and dark-field TEM (BF- and DF-XTEM) images of $ZrB_{2.18}$, $Zr_{0.87}Cr_{0.13}B_{2.92}$, $Zr_{0.46}Cr_{0.54}B_{2.40}$, $Zr_{0.10}Cr_{0.90}B_{1.81}$, and $CrB_{1.81}$ thin films, with corresponding selected area electron diffraction (SAED) patterns, are compared in Fig. 5. The BF- and DF-XTEM images of $ZrB_{2.18}$ in Fig. 5(a) and 5(f) show that the DCMS-grown $ZrB_{2.18}$ thin film has a columnar nanostructure with porosities, which are marked with white arrows in Fig. 5(a). The $ZrB_{2.18}$ columns are continual from close to the substrate to the surface and inclined ($\alpha = \sim 7^{\circ}$). This is attributed to the conservation of incident flux momentum component parallel to the film surface (the angle between the substrate and the ZrB_2 target is 21°) in combination with limited surface diffusion. The corresponding SAED pattern of $ZrB_{2.18}$ in Fig. 5(k) has diffraction rings with (0001), $(10\overline{1}0)$, and $(10\overline{1}1)$ components. The (0001) component has the weakest intensity, while $(10\overline{1}1)$ is the strongest one, in agreement with the XRD θ-2θ pattern of $ZrB_{2.18}$ shown in Fig. 3(a).

The BF- and DF-XTEM images of the $Zr_{0.87}Cr_{0.13}B_{2.92}$ alloy film, Fig. 5(b) and 5(g), show that the concurrent metal ion irradiation achieved by the hybrid CrB_2-HiPIMS/ZrB_2-DCMS co-sputtering in this compositional range, $x < 0.3$, is not sufficient to interrupt the continuous columnar growth. As a result, the films exhibit open porosities, marked with arrows, which develop due to the surface roughness evident in the SEM images in Fig. 4(b) and 4(h), and correspondently have high oxygen concentrations (~2.1 at. %). The SAED pattern of $Zr_{0.87}Cr_{0.13}B_{2.92}$, Fig. 5 (l), consists of diffraction arcs with (0001), $(10\overline{1}0)$, and $(10\overline{1}1)$ components, in which the $(10\overline{1}0)$ reflection has the weakest intensity. This SAED pattern also shows a change in the crystal orientation from predominant $(10\overline{1}1)$ for $ZrB_{2.18}$ to $(000l)$ for $Zr_{0.87}Cr_{0.13}B_{2.92}$.

In contrast, the $Zr_{1-x}Cr_xB_y$ alloy films with $x > 0.3$, represented by $Zr_{0.46}Cr_{0.54}B_{2.40}$ have a dense nanostructure with very fine columns. These columns do not extend throughout the whole layer (the continuous columnar growth is interrupted), Fig. 5(c) and 5(h). Thus, in the range of x values for which the films are dense, the ion fluxes relative to the ZrB_x deposition rate are sufficiently high to cause recoil density that it eliminates porosity and results in re-nucleation in the column growth, which in turn maintains the film's surface smooth [51,52]. Its SAED pattern is composed of (0001), $(10\overline{1}0)$, and $(10\overline{1}1)$ diffraction spots with a pronounced $000l$ fiber texture. The BF- and DF-XTEM images of $Zr_{0.10}Cr_{0.90}B_{1.81}$ in Fig. 5(d) and 5(i) confirm that this alloy has a dense crystalline columnar nanostructure with columns that appear wider than those of $Zr_{0.46}Cr_{0.54}B_{2.40}$. The reflections in the $Zr_{0.10}Cr_{0.90}B_{1.81}$ SAED pattern arise from the (0001), $(10\overline{1}0)$, and $(10\overline{1}1)$ planes with pronounced $000l$ orientation, Fig. 5(n), in agreement with its XRD θ-2θ signature in Fig. 3(i).

Parallel to $ZrB_{2.18}$, the DCMS-grown $CrB_{1.81}$ thin film has a porous columnar nanostructure, Fig. 5(e) and 5(j). The $CrB_{1.81}$ columns are tilted toward the CrB_2 target. The corresponding SAED pattern shown in Fig. 5(o) has diffraction rings with the (0001), $(10\overline{1}0)$, and $(10\overline{1}1)$ reflections, in which the (0001) reflection has the strongest intensity.

Fig. 6 shows the plan-view BF- and DF-TEM images of $ZrB_{2.18}$, $Zr_{0.87}Cr_{0.13}B_{2.92}$, $Zr_{0.46}Cr_{0.54}B_{2.40}$, $Zr_{0.10}Cr_{0.90}B_{1.81}$, and $CrB_{1.81}$ thin films. The column boundaries of $ZrB_{2.18}$ and $Zr_{0.87}Cr_{0.13}B_{2.92}$ in Fig. 6(a) and 6(b) appear bright, revealing porosities. Compared to $ZrB_{2.18}$ and $Zr_{0.87}Cr_{0.13}B_{2.92}$, the plan-view BF-TEM images of the $Zr_{0.46}Cr_{0.54}B_{2.40}$ and $Zr_{0.10}Cr_{0.90}B_{1.81}$ alloy films, Fig. 6(c) and 6(d), do not show bright column boundaries and instead, exhibit dense nanostructures with point-defect clusters induced due to ion irradiation during film growth. The $CrB_{1.81}$ thin film has a porous nanostructure, indicated with arrows in Fig. 6(e). In agreement with the XTEM micrographs in Fig. 4, the

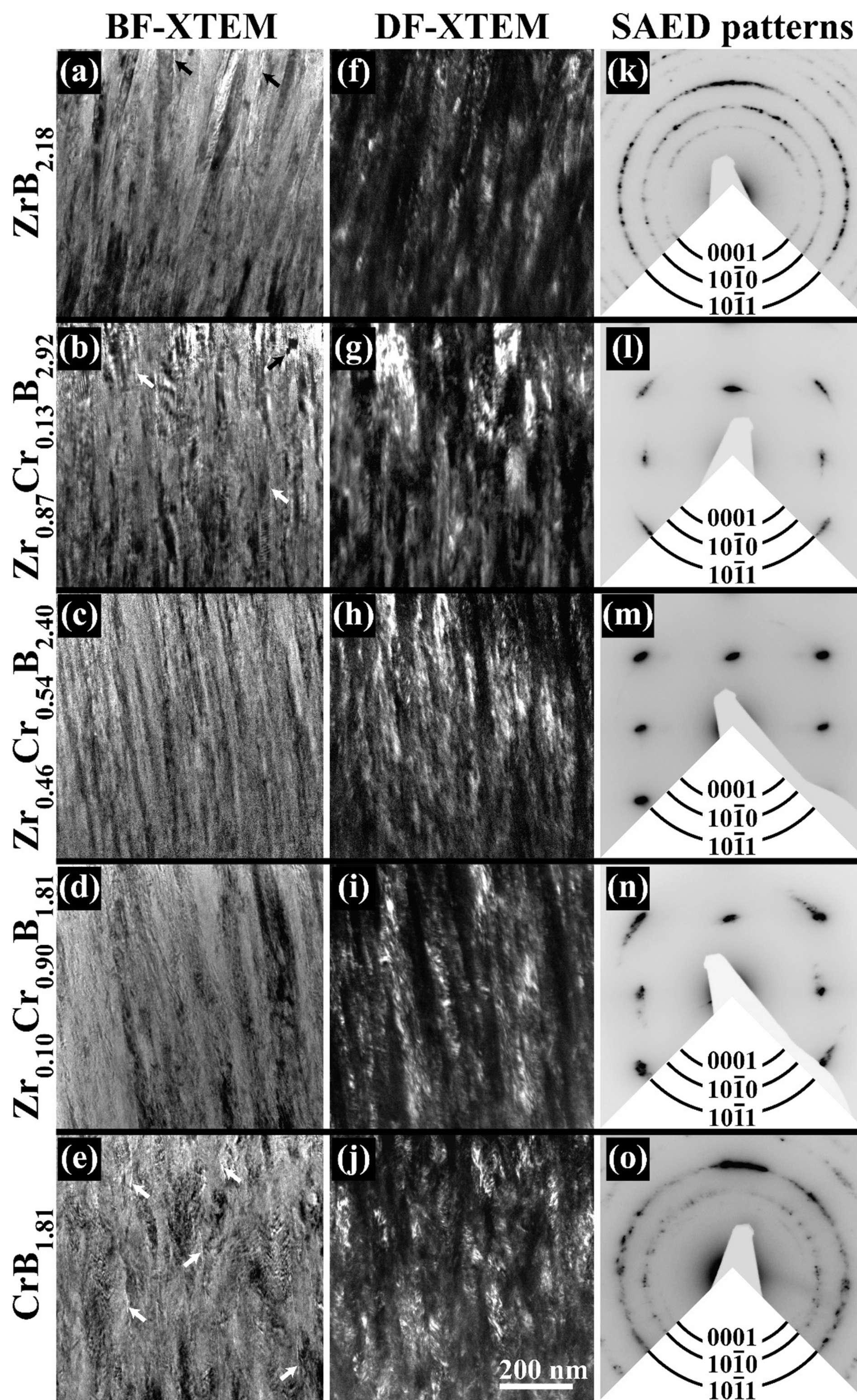

Fig. 5. BF- and DF-XTEM images with corresponding SAED patterns of (a, f, and k) $ZrB_{2.18}$, (b, g, and l) $Zr_{0.87}Cr_{0.13}B_{2.92}$, (c, h, and m) $Zr_{0.46}Cr_{0.54}B_{2.40}$, (d, i, and n) $Zr_{0.10}Cr_{0.90}B_{1.81}$, and (e, j, and o) $CrB_{1.81}$ thin films. Arrows in (a, b, and e) indicate porosities along the column boundaries.

$Zr_{0.87}Cr_{0.13}B_{2.92}$ alloy film together with the reference $ZrB_{2.18}$ and $CrB_{1.81}$ layers show open grain boundaries, marked with arrows. Average column widths, determined from DF-TEM images, are relatively large for the rough films with continuous columns: 20 ± 8 nm for $ZrB_{2.18}$, 27 ± 11 nm for $Zr_{0.87}Cr_{0.13}B_{2.92}$, and 35 ± 9 nm for $CrB_{1.81}$, while they smaller values for dense films with column re-nucleation: 8 ± 3 nm for $Zr_{0.46}Cr_{0.54}B_{2.40}$, and 17 ± 6 nm for $Zr_{0.10}Cr_{0.90}B_{1.81}$.

3.2. Mechanical properties

Fig. 7 shows the H and E values of the $Zr_{1-x}Cr_xB_y$ thin films as a function of x. The H value of $ZrB_{2.18}$ grown by DCMS using −100 V

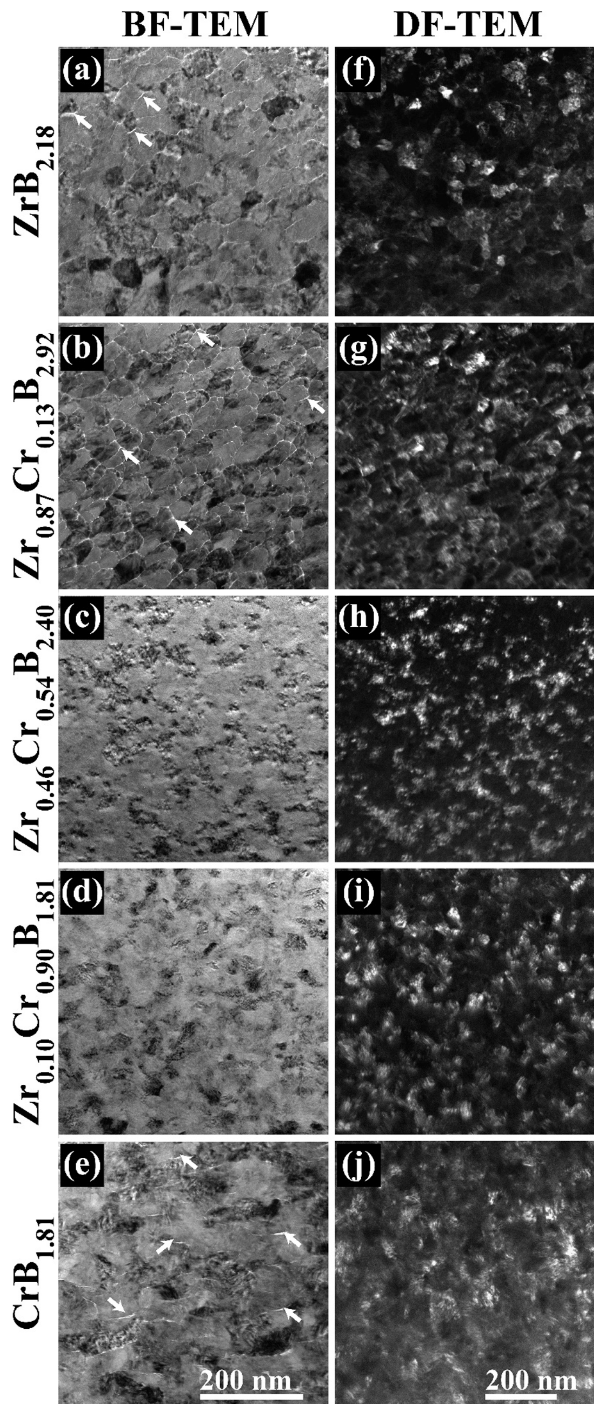

Fig. 6. Plan-view BF- and DF-TEM images of (a and f) $ZrB_{2.18}$, (b and g) $Zr_{0.87}Cr_{0.13}B_{2.92}$, (c and h) $Zr_{0.46}Cr_{0.54}B_{2.40}$, (d and i) $Zr_{0.10}Cr_{0.90}B_{1.81}$, and (e and j) $CrB_{1.81}$ thin films. Arrows in (a, b, and e) points to porosity.

substrate potential is 30.0 ± 1.0 GPa, while the $ZrB_{3.2}$ film grown by DCMS at floating substrate potential has an H value of 22.0 ± 1.0 GPa. The H values of the $Zr_{1\text{-}x}Cr_xB_y$ alloy films increases from 27.0 ± 1.4 GPa for $Zr_{0.87}Cr_{0.13}B_{2.92}$, to 27.5 ± 2.1 GPa for $Zr_{0.83}Cr_{0.17}B_{2.90}$, to 29.0 ± 2.0 GPa for $Zr_{0.76}Cr_{0.24}B_{2.81}$, to 32.5 ± 1.5 GPa for $Zr_{0.68}Cr_{0.32}B_{2.80}$. However, adding more CrB_y results in a slight decrease in H to 31.5 ± 1.9 GPa for $Zr_{0.57}Cr_{0.43}B_{2.50}$, 30.5 ± 2.0 GPa for $Zr_{0.46}Cr_{0.54}B_{2.40}$, 30.0 ± 1.4 GPa for $Zr_{0.30}Cr_{0.70}B_{2.14}$, and 29.0 ± 1.5 GPa for $Zr_{0.10}Cr_{0.90}B_{1.81}$. The $CrB_{1.81}$ thin film deposited by DCMS using −100 V substrate potential has an H value of 25.5 ± 2.0 GPa, whereas the hardness of $CrB_{1.7}$ grown by DCMS at floating substrate potential is 20.5 ± 1.2 GPa.

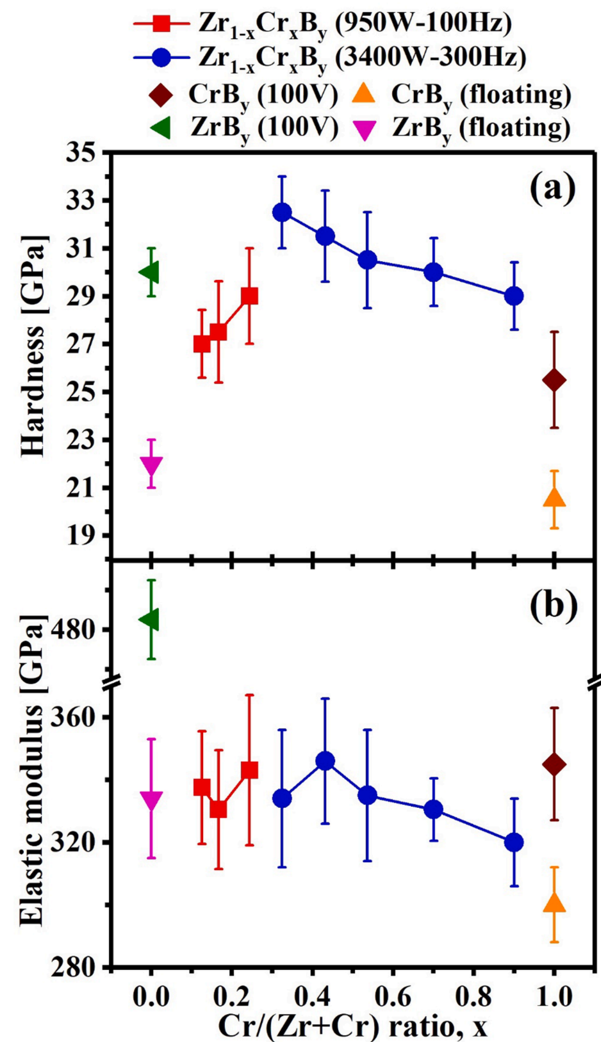

Fig. 7. (a) Nanoindentation H and (b) E values of $Zr_{1\text{-}x}Cr_xB_y$ thin films as a function of x ranging from 0 to 1.0.

The H(x) plot shown in Fig. 7 is the effect of two factors. First, in the range $x < 0.32$, the films are underdense, as evidenced by higher oxygen content (Fig. 2) and their cross-sectional and plan-view TEM images (Figs. 5 and 6), which results in lower H values. The layers with $0.32 \leq x \leq 0.9$ are dense (deposited at higher substrate potential duty cycle of 3%), and the decreasing trend in H is due to that the hardness of $CrB_{1.81}$ (25.5 ± 2.0 GPa) is lower than that of $ZrB_{2.18}$ (30.0 ± 1.0 GPa). Hence, the maximum hardness obtained for $Zr_{0.68}Cr_{0.32}B_{2.80}$ can be attributed to its dense nanostructure, highest Zr content of all dense alloys, solid solution hardening [53], and narrow column widths (based on Hall-Petch effect [54,55]).

The elastic moduli of the $ZrB_{2.18}$ and $CrB_{1.81}$ thin films grown using −100 V substrate potential are 485 ± 20 GPa and 345 ± 19 GPa, respectively, while the $ZrB_{3.2}$ and $CrB_{1.7}$ films deposited at floating substrate potential are 345 ± 18 GPa and 300 ± 12 GPa, respectively. The alloy films show lower E values than the reference layers fluctuating between 320 GPa and 345 GPa. Analogous to their H values, the $Zr_{1\text{-}x}Cr_xB_y$ alloy films exhibit close elastic moduli.

The in-plane residual stress σ_f of the films decreases from + 1.68 ± 0.07 GPa for $ZrB_{2.18}$, to + 1.65 ± 0.08 GPa for $Zr_{0.87}Cr_{0.13}B_{2.92}$, to + 0.11 ± 0.06 GPa for $Zr_{0.68}Cr_{0.32}B_{2.80}$, to + 0.05 ± 0.07 GPa for $Zr_{0.46}Cr_{0.54}B_{2.40}$, to −0.26 ± 0.15 GPa for $Zr_{0.10}Cr_{0.90}B_{1.81}$ (see Fig. 8). Then, it slightly increases to + 0.16 ± 0.07 GPa for the $CrB_{1.81}$ layer. The σ_f values are corrected for thermal stresses σ_{th} due to cooling the films

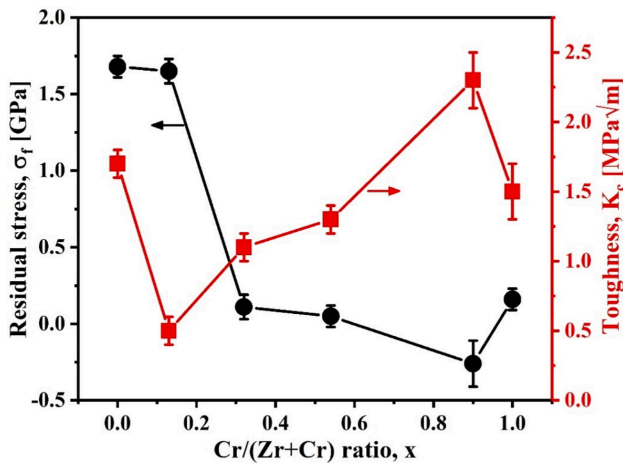

Fig. 8. In-plane residual stress σ_f and relative cube-corner nanoindentation toughness K_c values of $ZrB_{2.18}$, $Zr_{0.87}Cr_{0.13}B_{2.92}$, $Zr_{0.68}Cr_{0.32}B_{2.80}$, $Zr_{0.46}Cr_{0.54}B_{2.40}$, $Zr_{0.10}Cr_{0.90}B_{1.81}$, and $CrB_{1.81}$ thin films.

from deposition temperature to room temperature, $\Delta T = 450$ K, using the equation [56];

$$\sigma_{th} = \left[E\left(\alpha_f - \alpha_s\right)\Delta T\right]/(1-\nu), \tag{1}$$

in which α_f and α_s are thermal expansion coefficients of film and substrate, respectively. The thermal expansion coefficient α_s of Al_2O_3 is 8.1 $\times 10^{-6}$ K^{-1} [57]. For the $Zr_{1-x}Cr_xB_y$ alloy films, α_f is estimated from a linear interpolation between the thermal expansion coefficients of ZrB_2 (5.9×10^{-6} K^{-1}) and CrB_2 (10.5×10^{-6} K^{-1}) [58], and using elastic moduli E determined by nanoindentation. σ_{th} increases from −0.562 GPa for $ZrB_{2.18}$, to −0.286 GPa for $Zr_{0.87}Cr_{0.13}B_{2.92}$, −0.106 GPa for $Zr_{0.68}Cr_{0.32}B_{2.80}$, to + 0.053 GPa for $Zr_{0.46}Cr_{0.54}B_{2.40}$, to + 0.372 GPa for $Zr_{0.10}Cr_{0.90}B_{1.81}$, to + 0.476 GPa for $CrB_{1.81}$. The high tensile residual stress observed in the films with $x < 0.32$ is mainly due to their porous nanostructure and open column boundaries [59,60] and high surface roughness [61]. However, for the alloys with $x \geq 0.32$ several effects simultaneously result in their low residual stresses (almost stress free layers) such as the formation of dense nanostructure [62], ion-induced lattice damages [63,64], the crystal orientation change [65] as shown in the XRD data in Fig. 3, the incorporation of Cr atoms, which have smaller covalent radius than Zr atoms [66], in the diboride structure, and the decrease in the column widths [67].

The relative cube-corner nanoindentation toughness K_c of $ZrB_{2.18}$, $Zr_{0.87}Cr_{0.13}B_{2.92}$, $Zr_{0.68}Cr_{0.32}B_{2.80}$, $Zr_{0.46}Cr_{0.54}B_{2.40}$, $Zr_{0.10}Cr_{0.90}B_{1.81}$, and $CrB_{1.81}$ thin films grown on $Al_2O_3(0001)$ substrates are determined via the equation [68];

$$K_c = \alpha(E/H)^{0.5}\left(P/C_m^{1.5}\right), \tag{2}$$

in which α is the indenter geometry coefficient, 0.0319 [69]; C_m is the average length of radial cracks around a cube-corner indent; and P is the applied load. This equation was initially derived for bulk materials with infinite thicknesses [68,70]. Thus, for ceramic coatings, the coating thickness and substrate effects must be accounted for. One approach is to measure K_c at different loads, plot the K_c values as a function of maximum indentation penetration depth h_{max}, and then extrapolate the results to $h_{max} = 0$ [71]. Fig. 8 shows the K_c values of the $Zr_{1-x}Cr_xB_y$ thin films, determined using this approach, as a function of x. A range of loads from 10 to 50 mN is used for determining different K_c. The K_c value decreases from 1.7 ± 0.1 MPa$\sqrt{m}$ for $ZrB_{2.18}$ to 0.5 ± 0.1 MPa$\sqrt{m}$ for $Zr_{0.87}Cr_{0.13}B_{2.92}$, and then it increases to 1.1 ± 0.1 MPa$\sqrt{m}$ for $Zr_{0.68}Cr_{0.32}B_{2.80}$, 1.3 ± 0.1 MPa$\sqrt{m}$ for $Zr_{0.46}Cr_{0.54}B_{2.40}$ and 2.3 ± 0.2 MPa$\sqrt{m}$ for $Zr_{0.10}Cr_{0.90}B_{1.81}$. The $CrB_{1.81}$ thin film has a K_c of 1.5 ± 0.2 MPa$\sqrt{m}$.

Fig. 9 compares the plan-view SEM images from the cube-corner nanoindented $ZrB_{2.18}$, $Zr_{0.87}Cr_{0.13}B_{2.92}$, $Zr_{0.46}Cr_{0.54}B_{2.40}$, $Zr_{0.10}Cr_{0.90}B_{1.81}$, and $CrB_{1.81}$ thin films, grown on $Al_2O_3(0001)$ substrates, using a load of 50 mN. The average radial-crack length increases from $C_m = 2240 \pm 100$ nm for $ZrB_{2.18}$, to 2920 ± 290 nm for $Zr_{0.87}Cr_{0.13}B_{2.92}$, and then, it significantly decreases to 1950 ± 240 nm for $Zr_{0.46}Cr_{0.54}B_{2.40}$ and 1620 ± 130 nm for $Zr_{0.10}Cr_{0.90}B_{1.81}$. The $CrB_{1.81}$ thin film has a C_m of 2260 ± 180 nm. Compared to $ZrB_{2.18}$, $Zr_{0.87}Cr_{0.13}B_{2.92}$, and $CrB_{1.81}$, a significant pileup can be observed around the induced nanoindentation impressions of $Zr_{0.46}Cr_{0.54}B_{2.40}$ and $Zr_{0.10}Cr_{0.90}B_{1.81}$ alloy films, which proves their higher ductility.

3.3. Corrosion properties

Fig. 10 compares the potentiodynamic polarization curves of $ZrB_{2.18}$, $Zr_{0.87}Cr_{0.13}B_{2.92}$, $Zr_{0.46}Cr_{0.54}B_{2.40}$, $Zr_{0.10}Cr_{0.90}B_{1.81}$, and $CrB_{1.81}$ thin films in a 1.0 M NaCl corrosive aqueous medium. The corrosion potentials (E_{corr}), corrosion current densities (i_{corr}), and passive current densities (i_{pass}) determined from the polarization curves are summarized in Table 1. All layers exhibit high corrosion resistance with a very low dissolving rate across their anodic polarization curves. The i_{corr} value, which is considered as an indicator for corrosion rate, significantly decreases from $(3.0 \pm 0.4) \times 10^{-6}$ mA/cm^2 for $ZrB_{2.18}$ and $(8.2 \pm 0.7) \times 10^{-6}$ mA/cm^2 for $Zr_{0.87}Cr_{0.13}B_{2.92}$ to $(1.0 \pm 0.3) \times 10^{-6}$ mA/cm^2 for $Zr_{0.46}Cr_{0.54}B_{2.40}$. However, it increases to $(2.1 \pm 0.3) \times 10^{-6}$ mA/cm^2 for $Zr_{0.10}Cr_{0.90}B_{1.81}$ and $(4.3 \pm 0.5) \times 10^{-6}$ mA/cm^2 for $CrB_{1.81}$. The anodic polarization curves of $ZrB_{2.18}$, $Zr_{0.87}Cr_{0.13}B_{2.92}$, and $Zr_{0.46}Cr_{0.54}B_{2.40}$ consist of passive regions formed at ∼ 210 mV for $ZrB_{2.18}$ and $Zr_{0.87}Cr_{0.13}B_{2.92}$ and at ∼ 450 mV for $Zr_{0.46}Cr_{0.54}B_{2.40}$. The passive current density i_{pass} is $(2.3 \pm 0.2) \times 10^{-3}$ mA/cm^2 for $ZrB_{2.18}$ and $Zr_{0.87}Cr_{0.13}B_{2.92}$, while i_{pass} is $(1.3 \pm 0.3) \times 10^{-3}$ mA/cm^2 for $Zr_{0.46}Cr_{0.54}B_{2.40}$. In contrast, both $Zr_{0.10}Cr_{0.90}B_{1.81}$ and $CrB_{1.81}$ do not show any passivity up to 1200 mV and follow dominant Tafel behavior.

The electrochemical behavior of the coatings is further studied using EIS measurements in the 1.0 M NaCl corrosive medium. The Nyquist and Bode curves of $ZrB_{2.18}$, $Zr_{0.87}Cr_{0.13}B_{2.92}$, $Zr_{0.46}Cr_{0.54}B_{2.40}$, $Zr_{0.10}Cr_{0.90}B_{1.81}$, and $CrB_{1.81}$ thin films are plotted in Fig. 11. All Nyquist plots in Fig. 11(a) show single imperfect semicircles with the smallest radius for $Zr_{0.87}Cr_{0.13}B_{2.92}$, and the largest radii for $Zr_{0.46}Cr_{0.54}B_{2.40}$ and $Zr_{0.10}Cr_{0.90}B_{1.81}$. These plots indicate that there is no other capacitive loops or linear tails in low frequency range. The impedance spectra are fitted to a simple equivalent circuit, inset in Fig. 11(a), which is composed of a constant phase element (CPE), polarization resistance (R_p), and solution resistance (R_s). CPE indicates a double layer capacitance in parallel with R_p. In general, CPE is a non-ideal capacitance that is extensively employed to mimic the defective dielectric behavior. The CPE values are calculated by the equation [72];

$$CPE = P^{1/n} \bullet R_p^{(1-n)/n}, \tag{3}$$

where P is the magnitude of CPE and n is the deviation parameter. The equivalent circuit reveals that all layers follow a charge-transfer-controlled process in 1.0 M NaCl, while there are no other elements associated with a diffusion-controlled process. Table 2 lists the impedance parameters of the equivalent circuit that are quantitatively determined from the experimental data. The polarization resistance markedly increases from $R_p = 3.0$ MΩ.cm^2 for $ZrB_{2.18}$ and $R_p = 1.5$ MΩ.cm^2 for $Zr_{0.87}Cr_{0.13}B_{2.92}$ to $R_p = 25.0$ MΩ.cm^2 for $Zr_{0.46}Cr_{0.54}B_{2.4}$, with a simultaneous decrease in their capacitance, demonstrating a significant enhancement in the corrosion resistance. However, it decreases to $R_p = 20.0$ MΩ.cm^2 and 3.1 MΩ.cm^2 for $Zr_{0.10}Cr_{0.90}B_{1.81}$ and $CrB_{1.81}$, respectively.

Fig. 11(b) and 11(c) compare the Bode phase angle and impedance plots of $ZrB_{2.18}$, $Zr_{0.87}Cr_{0.13}B_{2.92}$, $Zr_{0.46}Cr_{0.54}B_{2.40}$, $Zr_{0.10}Cr_{0.90}B_{1.81}$, and $CrB_{1.81}$ thin films. Fig. 11(b) shows that the phase angles of all layers are close to 90° due to their high polarization resistance. All films exhibit

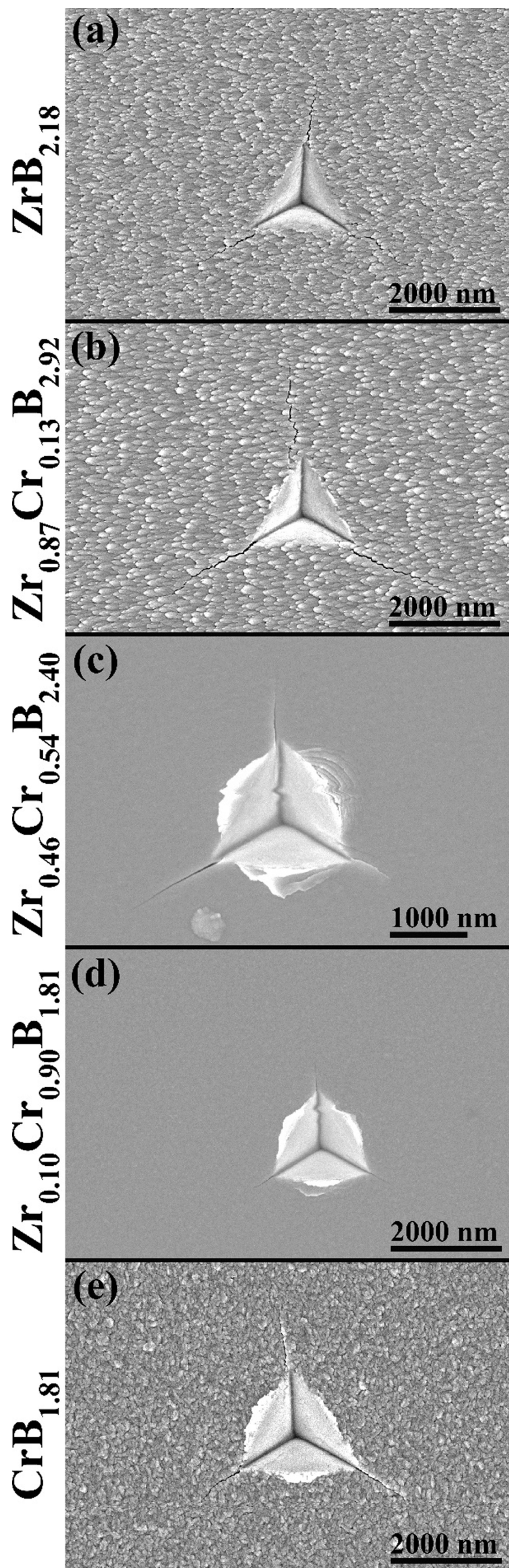

Fig. 9. SEM images acquired from the cube-corner nanoindented (a) $ZrB_{2.18}$, (b) $Zr_{0.87}Cr_{0.13}B_{2.92}$, (c) $Zr_{0.46}Cr_{0.54}B_{2.40}$, (d) $Zr_{0.10}Cr_{0.90}B_{1.81}$, and (e) $CrB_{1.81}$ thin films.

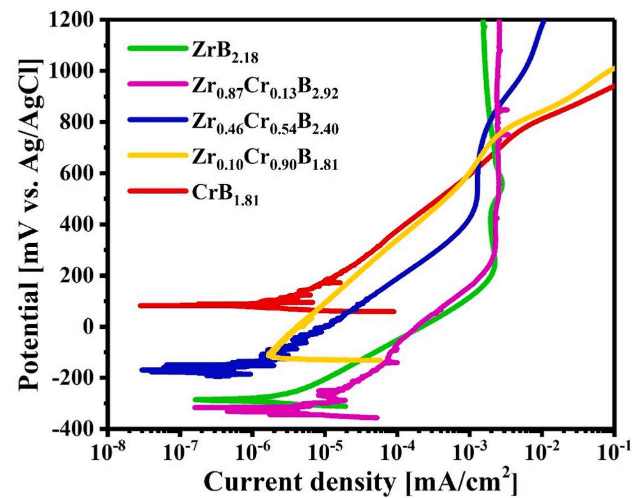

Fig. 10. Potentiodynamic polarization curves of $ZrB_{2.18}$, $Zr_{0.87}Cr_{0.13}B_{2.92}$, $Zr_{0.46}Cr_{0.54}B_{2.40}$, $Zr_{0.10}Cr_{0.90}B_{1.81}$, and $CrB_{1.81}$ thin films obtained in the aqueous 1.0 M NaCl corrosive medium.

Table 1
Corrosion potentials (E_{corr}), corrosion current densities (i_{corr}), and passive current densities (i_{pass}) of $ZrB_{2.18}$, $Zr_{0.87}Cr_{0.13}B_{2.92}$, $Zr_{0.46}Cr_{0.54}B_{2.40}$, $Zr_{0.10}Cr_{0.90}B_{1.81}$, and $CrB_{1.81}$ thin films after immersing in the 1.0 M NaCl corrosive medium.

	E_{corr} [mV vs. Ag/AgCl]	i_{corr} [$\times 10^{-6}$ mA/cm^2]	i_{pass} [$\times 10^{-3}$ mA/cm^2]
$ZrB_{2.18}$	−300 ± 34	3.0 ± 0.4	2.3 ± 0.2
$Zr_{0.87}Cr_{0.13}B_{2.92}$	−344 ± 41	8.2 ± 0.7	2.3 ± 0.2
$Zr_{0.46}Cr_{0.54}B_{2.40}$	−193 ± 22	1.0 ± 0.3	1.3 ± 0.3
$Zr_{0.10}Cr_{0.90}B_{1.81}$	−84 ± 29	2.1 ± 0.3	–
$CrB_{1.81}$	70 ± 25	4.3 ± 0.5	–

high impedance values in the low-frequency range, see Fig. 11(c), indicating good corrosion resistance.

Both reference DCMS $ZrB_{2.18}$ and $CrB_{1.81}$ thin films exhibit comparably high corrosion resistance. In addition, alloying ZrB_y layers with CrB_y using the hybrid CrB_2-HiPIMS/ZrB_2-DCMS co-sputtering does not have a considerable influence on the corrosion resistance of the $Zr_{1-x}Cr_xB_y$ thin films with $x \leq 0.13$. Plan-view and cross-sectional SEM and TEM images in Figs. 4, 5, and 6 show that the reference layers and the alloy films with $x \leq 0.13$ have rough surfaces and porous columnar structures in which the columns are extended along the films. Such structural properties may make these thin films susceptible to corrosion attacks. The potentiodynamic polarization and EIS results summarized in Tables 1 and 2 prove that $ZrB_{2.18}$, $CrB_{1.81}$, and $Zr_{0.87}Cr_{0.13}B_{2.92}$ have higher corrosion rates than the other alloys.

However, the $Zr_{1-x}Cr_xB_y$ alloys with ≥ 0.32 exhibit considerably better corrosion resistance. The corrosion resistance of $Zr_{0.46}Cr_{0.54}B_{2.40}$ and $Zr_{0.10}Cr_{0.90}B_{1.81}$ thin films is above seven times higher than $ZrB_{2.18}$, $CrB_{1.81}$, and $Zr_{0.87}Cr_{0.13}B_{2.92}$, see Figs. 10 and 11 together with their polarization and EIS data in Tables 1 and 2. These impressive corrosion properties can be mainly attributed to their non-columnar growth, smooth surfaces, and fully-dense fine-grain microstructures. The other factor that also effectively improves the corrosion resistance of the alloys with ≥ 0.32 is their chemistry. These layers contain more Cr, but less B. As Zr and Cr are more noble elements with lower dissolving rates; thus, it can enhance the corrosion properties of these alloys. $Zr_{0.46}Cr_{0.54}B_{2.40}$ has the lowest corrosion rate ($i_{corr} = \sim 1.0 \times 10^{-6}$ mA/cm^2) over the entire compositional range studied here; however, this rate is almost twice as high as the corrosion rate of $Zr_{0.56}Cr_{0.44}B_{1.11}$ ($i_{corr} = \sim 0.54 \times 10^{-6}$ mA/cm^2) that has an amorphous nanostructure and very-low B concentration [18]. It is a good comparison that reveals the influence of

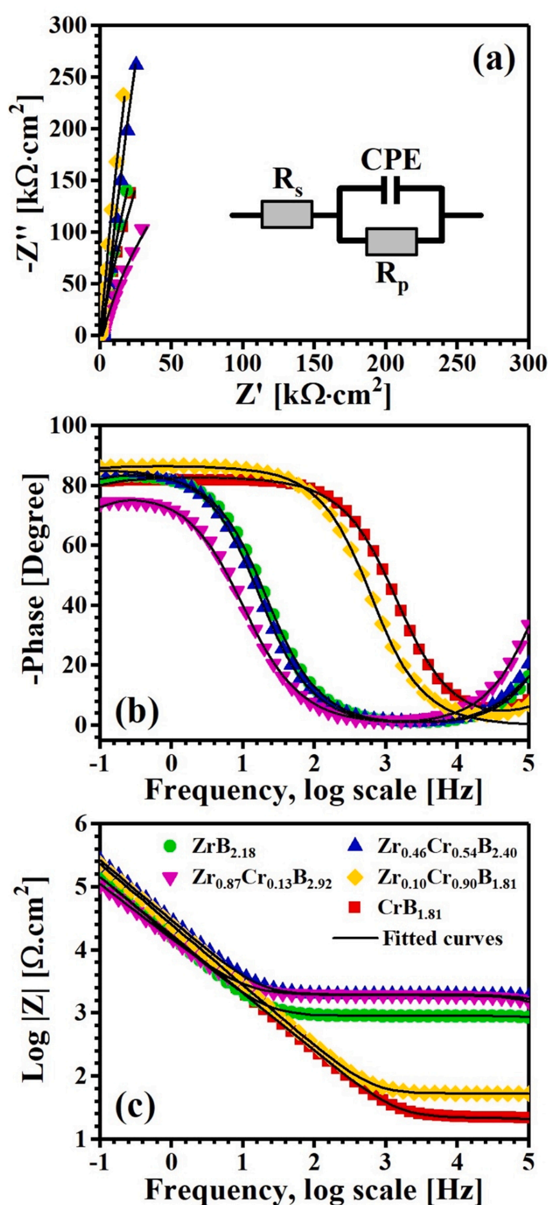

Fig. 11. (a) Nyquist and Bode (b) phase change and (c) impedance plots of $ZrB_{2.18}$, $Zr_{0.87}Cr_{0.13}B_{2.92}$, $Zr_{0.46}Cr_{0.54}B_{2.40}$, $Zr_{0.10}Cr_{0.90}B_{1.81}$, and $CrB_{1.81}$ thin films. The inset in (a) is the equivalent circuit model used to fit the EIS spectra.

Table 2
Impedance parameters extracted from fitting the EIS data using the equivalent circuit model.

	Rs ($\Omega.cm^2$)	Rp ($M\Omega.cm^2$)	CPE		C ($\mu F/cm^2$)
			P ($\mu F/cm^2$)	n	
$ZrB_{2.18}$	98	3.0	10.8	0.95	13.1
$Zr_{0.87}Cr_{0.13}B_{2.92}$	45	1.5	13.5	0.88	20.1
$Zr_{0.46}Cr_{0.54}B_{2.40}$	53	25.0	6.7	0.96	8.3
$Zr_{0.10}Cr_{0.90}B_{1.81}$	52	20.0	6.7	0.96	8.2
$CrB_{1.81}$	16	3.1	10.7	0.92	14.4

both chemistry and structure on the corrosion properties of diboride alloy thin films.

The slight decrease in the corrosion resistance together with the absence of the formation of the passive region in the anodic polarization curve of the $Zr_{0.10}Cr_{0.90}B_{1.81}$ alloy film, Fig. 10, can be primarily due to the intensive ion bombardment during the film growth that induces a large local distortions and residual strains in its crystal lattice, see Fig. 8. These regions with locally ion-induced strains can be highly prone to corrosion attacks and does not allow the passive-layer formation. On the other hand, the formation of the passive regions in the layers with $x \leq 0.54$ can be mostly attributed to the presence of diffusion-controlled zones, proved by the EIS measurements.

4. Conclusions

The use of the hybrid CrB_2-HiPIMS/ZrB_2-DCMS co-sputtering with Cr^+ ion bombardment changes the predominant crystallographic orientation from $(10\bar{1}1)$ for the DC-sputter-deposited reference $ZrB_{2.18}$ and $CrB_{1.81}$ thin films to $(000l)$ for the $Zr_{1-x}Cr_xB_y$ alloys. The columns of DCMS-grown $ZrB_{2.18}$ and $CrB_{1.81}$ are continual from the substrate to the surface with porous structure. We find that to eliminate pores and achieve dense alloy films, a critical intensity of the Cr^+-dominated ion flux, relative to the deposition rate from the ZrB_2 target, is required. Correspondingly, the films can be categorized in two group: (i) alloys with $x < 0.32$ that have continuous columnar growth, rough surfaces, and open column boundaries, and (ii) alloys with $x \geq 0.32$, where the intensity of Cr^+-dominated ion fluxes are sufficient to interrupt continuous column growth, which exhibits a smooth surface and dense fine-grain microstructure. The oxygen content in the underdense alloy films with $x < 0.32$ is in the range of 1.5–2 at. %, while it drops below 0.2 at. % for the alloy films with $x \geq 0.32$. The later number is significantly lower than the value of 1.5 at. % for the reference films deposited under continuous 100 eV Ar^+ bombardment in film densification. Compared to the porous films, the dense alloy films show higher hardness, in the range of 29.5–32.5 GPa. All porous films show tensile stress, while the dense alloy films are almost stress-free. In addition, they exhibit good average relative nanoindentation toughness of 1.3 MPa$\sqrt{m}$ to 2.3 MPa$\sqrt{m}$, and remarkedly low corrosion rates ($i_{corr} = \sim 1.0 \times 10^{-6}$ mA/cm^2 for $Zr_{0.46}Cr_{0.54}B_{2.40}$ and $i_{corr} = \sim 2.1 \times 10^{-6}$ mA/cm^2 for $Zr_{0.10}Cr_{0.90}B_{1.81}$).

These results reveal that the hybrid HiPIMS/DCMS co-sputtering technique provides energetic fluxes of metal ions resulting in dense TM diboride layers with smooth surfaces and a combination of favorable properties, similar to results previously reported for ternary TM nitrides. The hybrid technique is superior to DCMS. We find that a threshold ion flux density is required to achieve dense $Zr_{1-x}Cr_xB_y$ diboride thin films.

CRediT authorship contribution statement

Babak Bakhit: Conceptualization, Methodology, Investigation, Resources, Writing – original draft. **Samira Dorri:** Investigation, Writing – review & editing. **Ali Kosari:** Investigation, Writing – review & editing. **Arjan Mol:** Methodology, Writing – review & editing. **Ivan Petrov:** Conceptualization, Methodology, Writing – review & editing. **Jens Birch:** Conceptualization, Methodology, Writing – review & editing. **Lars Hultman:** Funding acquisition, Conceptualization, Methodology, Writing – review & editing. **Grzegorz Greczynski:** Conceptualization, Methodology, Writing – review & editing.

Declaration of Competing Interest

The authors declare that they have no known competing financial interests or personal relationships that could have appeared to influence the work reported in this paper.

Acknowledgments

We gratefully acknowledge financial support from Swedish Research Council VR Grant numbers 2018-03957, 2019-00191 (for accelerator-based ion-technological center in tandem accelerator laboratory in

Uppsala University), and 2021-00357, Swedish Energy Agency (Grant No. 51201-1), Swedish for Strategic Research (SSF), Swedish National Graduate School in Neutron Scattering (SwedNess), and Swedish Government Strategic Research Area in Materials Science on Advanced Functional Materials (AFM) at Linköping University (Faculty Grant SFO Mat LiU No.).

References

[1] W. Martienssen, H. Warlimont, Springer Handbook of Condensed Matter and Materials Data, Springer, Heidelberg, Berlin, 2006.

[2] T. Lundström, Transition metal borides, in: V.I. Matkovich (Ed.), Boron and Refractory Borides, Springer-Verlag, Heidelberg, Germany, 1977, pp. 351–376.

[3] A.L. Chamberlain, W.G. Fahrenholtz, G.E. Hilmas, D.T. Ellerby, High-Strength Zirconium Diboride-Based Ceramics, J. Am. Ceram. Soc. 87 (6) (2004) 1170–1172.

[4] B. Bakhit, D.L.J. Engberg, J. Lu, J. Rosen, H. Högberg, L. Hultman, I. Petrov, J. E. Greene, G. Greczynski, Strategy for simultaneously increasing both hardness and toughness in ZrB_2-rich $Zr_{1-x}Ta_xB_y$ thin films, J. Vac. Sci. Technol. A 37 (3) (2019) 031506, https://doi.org/10.1116/1.5093170.

[5] B. Bakhit, S. Mráz, J. Lu, J. Rosen, J.M. Schneider, L. Hultman, I. Petrov, G. Greczynski, Dense Ti0.67Hf0.33B1.7 thin films grown by hybrid HfB_2-HiPIMS/ TiB_2-DCMS co-sputtering without external heating, Vacuum 186 (2021) 110057, https://doi.org/10.1016/j.vacuum.2021.110057.

[6] B. Bakhit, J. Palisaitis, Z. Wu, M.A. Sortica, D. Primetzhofer, P.O.Å. Persson, J. Rosen, L. Hultman, I. Petrov, J.E. Greene, G. Greczynski, Age hardening in superhard ZrB_2-rich $Zr_{1-x}Ta_xB_y$ thin films, Scr. Mater. 191 (2021) 120–125.

[7] Y.M. Liu, R.Q. Han, F. Liu, Z.L. Pei, C. Sun, Sputtering gas pressure and target power dependence on the microstructure and properties of DC-magnetron sputtered AlB_2-type WB_2 films, J. Alloys Compd. 703 (2017) 188–197.

[8] Y. Liu, W. Shi, L.i. Tian, T. Li, C. Wang, F. Liu, Z. Pei, D.i. Fan, Influence of modulation period on structure and mechanical properties of WB_2/CrN films deposited by direct-current magnetron sputtering, J. Alloys Compd. 788 (2019) 729–738.

[9] W.G. Fahrenholtz, E.J. Wuchina, W.E. Lee, Y. Zhou, Ultra-high temperature ceramics: materials for extreme environment applications, John Wiley & Sons, 2014.

[10] W.G. Fahrenholtz, G.E. Hilmas, Ultra-high temperature ceramics: Materials for extreme environments, Scr. Mater. 129 (2017) 94–99.

[11] D.M. Van Wie, D.G. Drewry, D.E. King, C.M. Hudson, The hypersonic environment: Required operating conditions and design challenges, J. Mater. Sci. 39 (19) (2004) 5915–5924.

[12] N.P. Bansal, Handbook of ceramic composites, Kluwer Academic Publishers, Boston MA, 2005.

[13] JCPDS International Centre for Diffraction Data, Zirconium diboride (ZrB_2) card 00-034-0423.

[14] L. Bsenko, T. Lundström, The high-temperature hardness of ZrB_2 and HfB_2, J. Less. Common. Met. 34 (2) (1974) 273–278.

[15] N.P. Padture, Advanced structural ceramics in aerospace propulsion, Nat. Mater. 15 (2016) 804.

[16] T.A. Jackson, D.R. Eklund, A.J. Fink, High speed propulsion: Performance advantage of advanced materials, J. Mater. Sci. 39 (19) (2004) 5905–5913.

[17] D. Sziroczak, H. Smith, A review of design issues specific to hypersonic flight vehicles, Prog. Aerosp. Sci. 84 (2016) 1–28.

[18] B. Bakhit, S. Dorri, A. Kooijman, Z. Wu, J. Lu, J. Rosen, J.M.C. Mol, L. Hultman, I. Petrov, J.E. Greene, G. Greczynski, Multifunctional ZrB_2-rich $Zr_{1-x}Cr_xB_y$ thin films with enhanced mechanical, oxidation, and corrosion properties, Vacuum 185 (2021) 109990, https://doi.org/10.1016/j.vacuum.2020.109990.

[19] B. Bakhit, J. Palisaitis, P.O.Å. Persson, B. Alling, J. Rosen, L. Hultman, I. Petrov, J. E. Greene, G. Greczynski, Self-organized columnar $Zr_{0.7}Ta_{0.3}B_{1.5}$ core/shell-nanostructure thin films, Surf. Coat. Technol. 401 (2020), 126237.

[20] B. Bakhit, J. Palisaitis, J. Thörnberg, J. Rosen, P.O.Å. Persson, L. Hultman, I. Petrov, J.E. Greene, G. Greczynski, Improving the high-temperature oxidation resistance of TiB_2 thin films by alloying with Al, Acta Mater. 196 (2020) 677–689.

[21] B. Bakhit, I. Petrov, J.E. Greene, L. Hultman, J. Rosén, G. Greczynski, Controlling the B/Ti ratio of TiB_x thin films grown by high-power impulse magnetron sputtering, J. Vac. Sci. Technol. A 36 (3) (2018) 030604, https://doi.org/10.1116/1.5026445.

[22] J. Chrzanowska-Giżyńska, P. Denis, M. Giżyński, Ł. Kurpaska, I. Mihailescu, C. Ristoscu, Z. Szymański, T. Mościcki, Thin WB_x and $W_yTi_{1-y}B_x$ films deposited by combined magnetron sputtering and pulsed laser deposition technique, Appl. Surf. Sci. 478 (2019) 505–513.

[23] S. Mirzaei, M. Alishahi, P. Souček, V. Buršíková, L. Zábranský, L. Gröner, F. Burmeister, B. Blug, P. Daum, R. Mikšová, P. Vašina, Effect of substrate bias voltage on the composition, microstructure and mechanical properties of W-B-C coatings, Appl. Surf. Sci. 528 (2020), 146966.

[24] I. Campos, M. Palomar-Pardavé, A. Amador, C. VillaVelázquez, J. Hadad, Corrosion behavior of boride layers evaluated by the EIS technique, Appl. Surf. Sci. 253 (2007) 9061–9066.

[25] J. Yang, Z. Yang, X. Lei, J. Huang, S. Chen, Z. Ye, Y. Zhao, Behavior and mechanism for Boron atom diffusing across tungsten grain boundary in the preparation of WB coating: A first-principles calculation, Appl. Surf. Sci. 543 (2021), 148778.

[26] R. Psiuk, M. Milczarek, P. Jenczyk, P. Denis, D.M. Jarząbek, P. Bazarnik, M. Pisarek, T. Mościcki, Improved mechanical properties of W-Zr-B coatings deposited by hybrid RF magnetron - PLD method, Appl. Surf. Sci. 570 (2021), 151239.

[27] J.M. Johnston, S.A. Catledge, Metal-boride phase formation on tungsten carbide (WC-Co) during microwave plasma chemical vapor deposition, Appl. Surf. Sci. 364 (2016) 315–321.

[28] W.J. Clegg, Controlling Cracks in Ceramics, Science 286 (5442) (1999) 1097–1099.

[29] W.G. Fahrenholtz, G.E. Hilmas, I.G. Talmy, J.A. Zaykoski, Refractory Diborides of Zirconium and Hafnium, J. Am. Ceram. Soc. 90 (5) (2007) 1347–1364.

[30] J.K. Sonber, A.K. Suri, Synthesis and consolidation of zirconium diboride: review, Adv. Appl. Ceram. 110 (6) (2011) 321–334.

[31] T.A. Parthasarathy, R.A. Rapp, M. Opeka, R.J. Kerans, A model for the oxidation of ZrB_2, HfB_2 and TiB_2, Acta Mater. 55 (17) (2007) 5999–6010.

[32] J. Thörnberg, B. Bakhit, J. Palisaitis, N. Hellgren, L. Hultman, G. Greczynski, P.O. Å. Persson, I. Petrov, J. Rosen, Improved oxidation properties from a reduced B content in sputter-deposited TiB_x thin films, Surf. Coat. Technol. 420 (2021), 127353.

[33] C. Fuger, B. Schwartz, T. Wojcik, V. Moraes, M. Weiss, A. Limbeck, C.A. Macauley, O. Hunold, P. Polcik, D. Primetzhofer, P. Felfer, P.H. Mayrhofer, H. Riedl, Influence of Ta on the oxidation resistance of WB_{2-z} coatings, J. Alloys Compd. 864 (2021), 158121.

[34] G. Greczynski, I. Petrov, J.E. Greene, L. Hultman, Paradigm shift in thin-film growth by magnetron sputtering: From gas-ion to metal-ion irradiation of the growing film, J. Vac. Sci. Technol. A 37 (6) (2019), 060801.

[35] G. Greczynski, S. Mráz, J.M. Schneider, L. Hultman, Metal-ion subplantation: A game changer for controlling nanostructure and phase formation during film growth by physical vapor deposition, J. Appl. Phys. 127 (2020), 180901.

[36] G. Greczynski, L. Hultman, Peak amplitude of target current determines deposition rate loss during high power pulsed magnetron sputtering, Vacuum 124 (2016) 1–4.

[37] G. Greczynski, J. Lu, J. Jensen, I. Petrov, J.E. Greene, S. Bolz, W. Kölker, C. Schiffers, O. Lemmer, L. Hultman, Metal versus rare-gas ion irradiation during $Ti_{1-x}Al_xN$ film growth by hybrid high power pulsed magnetron/dc magnetron co-sputtering using synchronized pulsed substrate bias, J. Vac. Sci. Technol. A 30 (6) (2012) 061504, https://doi.org/10.1116/1.4750485.

[38] G.G. Stoney, C.A. Parsons, The tension of metallic films deposited by electrolysis, Proceedings of the Royal Society of London. Series A, Containing Papers of a Mathematical and Physical Character 82(553) (1909) 172-175.

[39] G.C.A.M. Janssen, M.M. Abdalla, F. van Keulen, B.R. Pujada, B. van Venrooy, Celebrating the 100th anniversary of the Stoney equation for film stress: Developments from polycrystalline steel strips to single crystal silicon wafers, Thin Solid Films 517 (6) (2009) 1858–1867.

[40] N.L. Okamoto, M. Kusakari, K. Tanaka, H. Inui, M. Yamaguchi, S. Otani, Temperature dependence of thermal expansion and elastic constants of single crystals of ZrB_2 and the suitability of ZrB_2 as a substrate for GaN film, J. Appl. Phys. 93 (1) (2003) 88–93.

[41] N.L. Okamoto, M. Kusakari, K. Tanaka, H. Inui, S. Otani, Anisotropic elastic constants and thermal expansivities in monocrystal CrB_2, TiB_2, and ZrB_2, Acta Mater. 58 (1) (2010) 76–84.

[42] G.M. Pharr, Measurement of mechanical properties by ultra-low load indentation, Mater. Sci. Eng. A 253 (1-2) (1998) 151–159.

[43] J.F. Ziegler, M.D. Ziegler, J.P. Biersack, SRIM – The stopping and range of ions in matter (2010), Nucl. Instrum. Methods Phys. Res. B 268 (11-12) (2010) 1818–1823.

[44] X. Li, B. Bakhit, M.P.J. Jõesaar, L. Hultman, I. Petrov, G. Greczynski, Toward energy-efficient physical vapor deposition: Routes for replacing substrate heating during magnetron sputter deposition by employing metal ion irradiation, Surf. Coat. Technol. 415 (2021), 127120.

[45] X. Li, B. Bakhit, M.P. Johansson Jõesaar, I. Petrov, L. Hultman, G. Greczynski, Towards energy-efficient physical vapor deposition: Mapping out the effects of W^+ energy and concentration on the densification of TiAlWN thin films grown with no external heating, Surf. Coat. Technol., 424 (2021) 127639.

[46] X. Li, B. Bakhit, M.P. Johansson Jõesaar, I. Petrov, L. Hultman, G. Greczynski, Dense, single-phase, hard, and stress-free $Ti_{0.32}Al_{0.63}W_{0.05}N$ films grown by magnetron sputtering with dramatically reduced energy consumption, Sci. Rep. 12 (2022) 2166.

[47] B. Bakhit, D. Primetzhofer, E. Pitthan, M.A. Sortica, E. Ntemou, J. Rosen, L. Hultman, I. Petrov, G. Greczynski, Systematic compositional analysis of sputter-deposited boron-containing thin films, J. Vac. Sci. Technol. A 39 (6) (2021) 063408, https://doi.org/10.1116/6.0001234.

[48] JCPDS International Centre for Diffraction Data, Chromium diboride (CrB_2) card 00-008-0119.

[49] P. Zaumseil, High-resolution characterization of the forbidden Si 200 and Si 222 reflections, J. Appl. Crystallogr. 48 (2) (2015) 528–532.

[50] G. Greczynski, J. Jensen, L. Hultman, Mitigating the geometrical limitations of conventional sputtering by controlling the ion-to-neutral ratio during high power pulsed magnetron sputtering, Thin Solid Films 519 (19) (2011) 6354–6361.

[51] G. Greczynski, J. Lu, O. Tengstrand, I. Petrov, J.E. Greene, L. Hultman, Nitrogen-doped bcc-Cr films: Combining ceramic hardness with metallic toughness and conductivity, Scr. Mater. 122 (2016) 40–44.

[52] I. Petrov, P.B. Barna, L. Hultman, J.E. Greene, Microstructural evolution during film growth, J. Vac. Sci. Technol. A 21 (5) (2003) S117–S128.

[53] G.E. Dieter, D.J. Bacon, Mechanical metallurgy, McGraw-hill NY (1986).

[54] E.O. Hall, The Deformation and Ageing of Mild Steel: III Discussion of Results, Proc. Phys. Soc. B 64 (9) (1951) 747–753.

[55] N.J. Petch, The Cleavage Strength of Polycrystals, J Iron Steel Inst. 174 (1953) 25–28.

[56] M. Ohring, Materials science of thin films, Academic Press, San Diego, California, 2001.
[57] E.R. Dobrovinskaya, L.A. Lytvynov, V. Pishchik, Sapphire: material, manufacturing, applications, Springer Science & Business Media, 2009.
[58] V.I. Matkovich, G.V. Samsonov, P. Hagenmuller, T. Lundstrom, Boron and refractory borides, Springer-Verlag, Berlin, 1977.
[59] G.C.A.M. Janssen, A.J. Dammers, V.G.M. Sivel, W.R. Wang, Tensile stress in hard metal films, Appl. Phys. Lett. 83 (16) (2003) 3287–3289.
[60] E. Chason, A kinetic analysis of residual stress evolution in polycrystalline thin films, Thin Solid Films 526 (2012) 1–14.
[61] A.J. Detor, A.M. Hodge, E. Chason, Y. Wang, H. Xu, M. Conyers, A. Nikroo, A. Hamza, Stress and microstructure evolution in thick sputtered films, Acta Mater. 57 (7) (2009) 2055–2065.
[62] Y. Pauleau, Generation and evolution of residual stresses in physical vapour-deposited thin films, Vacuum 61 (2-4) (2001) 175–181.
[63] R. Daniel, K.J. Martinschitz, J. Keckes, C. Mitterer, The origin of stresses in magnetron-sputtered thin films with zone T structures, Acta Mater. 58 (7) (2010) 2621–2633.
[64] M. Koster, H.M. Urbassek, Ion peening and stress relaxation induced by low-energy atom bombardment of covalent solids, Phy. Rev. B 63 (22) (2001), 224111.
[65] R. Daniel, K.J. Martinschitz, J. Keckes, C. Mitterer, Texture development in polycrystalline CrN coatings: the role of growth conditions and a Cr interlayer, J. Phys. D: Appl. Phys. 42 (7) (2009), 075401.
[66] L. Pauling, Atomic Radii and Interatomic Distances in Metals, J. Am. Chem. Soc. 69 (3) (1947) 542–553.
[67] D. Magnfält, A. Fillon, R.D. Boyd, U. Helmersson, K. Sarakinos, G. Abadias, Compressive intrinsic stress originates in the grain boundaries of dense refractory polycrystalline thin films, J. Appl. Phys. 119 (5) (2016) 055305, https://doi.org/10.1063/1.4941271.
[68] B.R. Lawn, A.G. Evans, D.B. Marshall, Elastic/Plastic Indentation Damage in Ceramics: The Median/Radial Crack System, J. Am. Ceram. Soc. 63 (9-10) (1980) 574–581.
[69] G.M. Pharr, D.S. Harding, W.C. Oliver, Measurement of Fracture Toughness in Thin Films and Small Volumes Using Nanoindentation Methods, in: M. Nastasi, D. M. Parkin, H. Gleiter (Eds.), Mechanical Properties and Deformation Behavior of Materials Having Ultra-Fine Microstructures, Springer, Netherlands, Dordrecht, 1993, pp. 449–461.
[70] G.R. Anstis, P. Chantikul, B.R. Lawn, D.B. Marshall, A Critical Evaluation of Indentation Techniques for Measuring Fracture Toughness: I, Direct Crack Measurements, J. Am. Ceram. Soc. 64 (9) (1981) 533–538.
[71] Y.X. Wang, S. Zhang, J.-W. Lee, W.S. Lew, B.o. Li, Influence of bias voltage on the hardness and toughness of CrAlN coatings via magnetron sputtering, Surf. Coat. Technol. 206 (24) (2012) 5103–5107.
[72] B. Hirschorn, M.E. Orazem, B. Tribollet, V. Vivier, I. Frateur, M. Musiani, Determination of effective capacitance and film thickness from constant-phase-element parameters, Electrochim. Acta 55 (21) (2010) 6218–6227.